American Mineralogist, Volume 108, pages 127–139, 2023

Potential link between antigorite dehydration and shallow intermediate-depth earthquakes in hot subduction zones

Tongbin Shao[1,2,3,*], Maoshuang Song[1,3,*], Xi Ma[2], Xing Ding[1,3], Shirong Liu[4], Yongsheng Zhou[2], Jie Wu[5], Xiaoning Wang[1,3], and Jianfeng Li[1,3]

[1]State Key Laboratory of Isotope Geochemistry, Guangzhou Institute of Geochemistry, Chinese Academy of Sciences, Guangzhou 510640, China
[2]State Key Laboratory of Earthquake Dynamics, Institute of Geology, China Earthquake Administration, Beijing 100029, China
[3]CAS Center for Excellence in Deep Earth Science, Guangzhou 510640, China
[4]State Key Laboratory of Environmental Geochemistry, Institute of Geochemistry, Chinese Academy of Sciences, Guiyang 550003, China
[5]College of Earth Sciences and Guangxi Key Laboratory of Hidden Metallic Ore Deposits Exploration, Guilin University of Technology, Guilin 541004, China

Abstract

The distribution of earthquakes at intermediate depths corresponding to pressures <2 GPa in several hot subduction zones (such as Cascadia and southwestern Japan) coincides with the breakdown of antigorite to forsterite and talc; thus, this reaction may have triggered these earthquakes. However, previous studies have overlooked the potential significance of this reaction. Here, we performed a series of time-dependent dehydration experiments on antigorite at a pressure of 200 MPa and a temperature range of 500–650 °C. The results show that dehydration is controlled by a heterogeneous nucleation and growth mechanism and has an activation energy of 354 ± 24 kJ/mol. The formation of fine-grained forsterite and large talc crystals is consistent with kinetic results indicating Avrami exponents n = ~1.4–1.1 and ~2.7, respectively. Fluid production rates at 600 and 650 °C are 2.54×10^{-6} and 4.69×10^{-5} $m^3_{fluid} m^{-3}_{rock} s^{-1}$, respectively, which are much faster than those of mantle deformation, causing high fluid pressure in hot subducting mantle but not necessarily embrittlement. We emphasize the role of kinetic mechanisms in controlling the grain sizes of reaction products, which likely determine the mechanical behavior of serpentinized fault zones. Superplasticity or velocity weakening of fine-grained forsterite and velocity weakening of antigorite by water and/or talc may be responsible for earthquake nucleation and propagation in a heterogeneous system, which can be either dehydration products within a serpentinized fault zone or the mixture of antigorite fault and surrounding peridotite in hot subduction zones (<2 GPa).

Keywords: Antigorite, talc, forsterite, kinetic mechanism, subduction zone, shallow intermediate-depth earthquakes

Introduction

Serpentine is a main hydrous phase in oceanic plates and the most abundant water-bearing mineral in altered ultramafic rocks (Hyndman and Peacock 2003), with water contents up to ~13 wt% (Schmidt and Poli 1998; Shao et al. 2014, 2021, 2022; Ulmer and Trommsdorff 1999). There are three main forms of serpentine: chrysotile, lizardite, and antigorite (Rinaudo et al. 2003). Among them, antigorite is persistent in subduction zones to a depth of ~200 km and is thus called high-temperature serpentine (Ji et al. 2013; Reynard 2013; Reynard et al. 2007; Shao et al. 2014). Previous studies have shown that the temperature stability field of antigorite, from 1 to 5 GPa, is close to the isotherm of the lower plane of a double seismic zone (DSZ) (e.g., Abers et al. 2013; Peacock 2001; Yamasaki and Seno 2003); which means that the hypocenter distribution of intermediate-depth earthquakes in the subducted mantle fits the distribution of antigorite. However, a recent study by Ferrand (2019) suggested that many of the upper-plane earthquakes actually appear in the uppermost mantle, as clearly observed in northern Chile. Therefore, antigorite dehydration is commonly used to explain the seismic activity in the entire DSZ (Dobson et al. 2002; Omori et al. 2004; Peacock 2001).

In a pioneering study by Raleigh and Paterson (1965), seismogenic faulting was claimed to be triggered within the dehydrating antigorite itself due to fluid overpressure. This is the original model of so-called "dehydration embrittlement," which is possible only when the Clapeyron slope of serpentine dehydration reaction is positive (i.e., at P < ~2 GPa). However, several experimental studies on syndeformational antigorite dehydration have found that antigorite is weakened but deforms aseismically (Chernak and Hirth 2010, 2011; Gasc et al. 2011, 2017; Okazaki and Hirth 2016; Proctor and Hirth 2015; Shao et al. 2021), which might be comparable to slow earthquakes occurring in hot subduction zones (e.g., Chernak and Hirth 2010; French et al. 2019; Okazaki and Katayama 2015). Some studies have improved the model and considered that seismogenic faulting should occur in more brittle surrounding rocks rather than the dehydrating antigorite itself (e.g., Brantut et al. 2017; Ferrand et al. 2017). For example, Ferrand et al. (2017) proposed dehydration-driven stress transfer (DDST) to generate earthquake events in fresh peridotite at the edge of antigorite-rich zones.

* E-mail: tshao2022@outlook.com (Orcid 0000-0001-5202-3464); msong@gig.ac.cn (Orcid 0000-0002-3006-756X)

0003-004X/23/0001–127$05.00/DOI: https://doi.org/10.2138/am-2022-8271

Downloaded from http://pubs.geoscienceworld.org/msa/ammin/article-pdf/108/1/127/5755349/am-2022-8271.pdf
by Institute of Geochemistry Chinese Academy user
on 12 June 2024

However, seismicity is triggered by dehydration of very limited amounts of antigorite (Ferrand et al. 2017; Xia 2013), implying that these earthquakes are not the result of fluid overpressure. Concurrently, Brantut et al. (2017) proposed a new dehydration embrittlement model, in which positive feedback between pore fluid pressure, shear compaction, and the dehydration rate of antigorite was considered to induce nucleation and propagation of earthquakes in the surrounding rocks forming the subducted slab. Thus, the role of fluid in triggering the lower plane earthquakes is still inconclusive. Furthermore, both the DDST and the new dehydration embrittlement models, unlike the original dehydration embrittlement, are specifically for the case where the net volume change of the dehydration reaction is negative. These facts suggest that none of the models can explain seismicity related to the dehydration reaction of antigorite with positive volume change, which is the reaction of antigorite breakdown to forsterite and talc.

To explain intermediate-depth earthquakes, several dehydration kinetics studies of serpentine minerals have been performed over the past two decades using various methods, such as time-resolved X-ray diffraction (XRD) (Chollet et al. 2011; Gualtieri et al. 2012; Inoue et al. 2009; Perrillat et al. 2005), high-temperature infrared microspectroscopy (Sawai et al. 2013), and thermogravimetric analysis (Balucan et al. 2011; Liu et al. 2019; Weber and Greer 1965). However, published conclusions regarding the kinetic mechanism are significantly different (Balucan et al. 2011; Gualtieri et al. 2012; Liu et al. 2019; Perrillat et al. 2005; Sawai et al. 2013). In addition, these studies were conducted under conditions of either ambient pressure (e.g., Liu et al. 2019; Sawai et al. 2013) or high pressures [e.g., 1.1–1.5 GPa in Perrillat et al. (2005) and ~4 GPa in Chollet et al. (2011)], but data under relatively low pressures (<1 GPa) are lacking. Furthermore, no microstructural observations of run products were performed in most of these previous studies to support the analyses of the kinetic mechanism of antigorite dehydration. These previous dehydration kinetics studies all suggest that antigorite dehydration can trigger earthquakes based on either the original dehydration embrittlement (related to fluid overpressure) (e.g., Chollet et al. 2011; Perrillat et al. 2005) or the DDST model (Liu et al. 2019). According to the results of syndeformational dehydration experiments with antigorite (e.g., Chernak and Hirth 2011; Gasc et al. 2011), however, fast fluid production rates calculated based on kinetic parameters alone cannot account for the potential link between antigorite dehydration and seismicity (e.g., Liu et al. 2019; Perrillat et al. 2005). The microstructural morphology (controlled by the kinetic mechanism) and thus, the mechanical behavior of reaction products should not be ignored. In addition, the reaction of antigorite breakdown to forsterite and talc has not yet been considered in most of these dehydration kinetics studies (e.g., Chollet et al. 2011; Inoue et al. 2009; Liu et al. 2019; Perrillat et al. 2005). This reaction fits the most shallow intermediate-depth seismicity in the hot subducting mantle beneath Cascadia and southwestern Japan (Abers et al. 2013; Ferrand 2019), indicating the geophysical significance of this dehydration reaction.

In this paper, high-pressure and high-temperature (high *P-T*) experiments were carried out on antigorite using a Tuttle-type autoclave (cold-seal hydrothermal vessel). Our goal is to study the dehydration kinetics of antigorite by isothermal experiments and analyze the kinetic mechanism by both Avrami modeling of the experimental data and microstructural observations of run products, which provide constraints on the fluid production rate and the mechanical behavior of run products, respectively. Finally, the experimental results are extrapolated to hot subduction zones ($P < 2$ GPa) to interpret the shallow intermediate-depth seismicity occurring in these zones by emphasizing the role of the kinetic mechanism in controlling the grain size and, thus, the mechanical behavior of dehydration products.

Methods

Starting material

The material used in the dehydration kinetics experiments is known as Xiuyan jade in Chinese culture, has a mineral composition of mainly antigorite with trace amounts of dolomite and apatite (<1%), and was collected from Xiuyan Manchu Autonomous County (Liaoning Province, China) (Shao et al. 2014, 2021, 2022). Whole-rock X-ray fluorescence (XRF) analyses reveal that the starting material contains 44.25 wt% SiO_2, 41.83 wt% MgO, 0.28 wt% CaO, 0.03 wt% Na_2O, 0.06 wt% Al_2O_3, 0.97 wt% TFeO (total iron given as FeO), and 12.19 wt% water. The nearly pure antigorite crystals were crushed and ground into powder with various grain sizes, from which mean particles of ~10–15 μm were selected and stored in a furnace at 110 °C, eliminating absorbed molecular water. To determine the structure of the starting material that may affect the phase stability and thus the dehydration kinetics, we investigated the starting material via XRD at the Institute of Geology, China Earthquake Administration (IGCEA), Beijing, and transmission electron microscopy (TEM) at the Institute of Geochemistry, Chinese Academy of Sciences (IGCAS), Guiyang, Guizhou Province. The TEM investigation was carried out on a suspension that was made according to the powder technique described by Shen et al. (2020).

The XRD analyses suggest that the starting material is characterized by lattice constants with $a = 5.42$, $b = 9.24$, $c = 7.27$ Å, and $\beta = 91.32°$. Figure 1 shows a high-resolution TEM image of a representative grain and a histogram of the *m* value, which is equal to $(a^*/5.42) \times 2 + 1$, where a^* is the length of the *a*-axis and 5.42 Å represents the length of the subcells along the *a*-axis in this material, that is, the lattice constant *a*. The *m* represents the number of tetrahedra in a single chain along the wavelength a^*. The results show that the *m* value ranges from 13 to 18, with the most frequent value being 15; thus, this value can be used as the polysome *m* value of the starting material.

High *P-T* experiments

All dehydration kinetics experiments were performed at a pressure of 200 MPa and temperatures of 500–650 °C with durations ranging from 1 to 745.5 h (Table 1) using a Tuttle-type autoclave (Online Materials Fig. S1) at the Guangzhou Institute of Geochemistry, Chinese Academy of Sciences (GIGCAS). The antigorite powder was loaded into gold capsules of two sizes: one had an outer diameter of 5.0 mm, and the other had an outer diameter of 4.6 mm. Both gold capsules had a wall thickness of 0.25 mm and a length of 18 mm. One side of a capsule was welded with a tungsten inert gas high-frequency pulse welder (PUK3, Lampert Werktechnik, Germany) before loading, and the other side was welded after loading with either just sample powder (the system was water unsaturated at least at the beginning of the experiment) or sample powder plus excess deionized water (the system was water saturated throughout the experiment). A leak check was performed before all experiments. For initially water-unsaturated samples, we immersed capsules in alcohol for at least 1 h and then placed them in a drying furnace at 110 °C for at least 2 h. For water-saturated samples, the capsules were directly placed in the drying furnace at 110 °C for at least 2 h. To determine whether the sample capsule was a closed or open system, the sealing conditions of the sample capsule had to be confirmed. Thus, it was necessary to weigh each sample capsule before and after the experiments; capsules with a weight difference of less than ~0.5 mg were considered completely sealed, which could be further supported by the increased widths of these capsules after removal from the vessels. Capsules whose shapes stayed the same as before the experiments were considered open, and the experimental results from capsules with this characteristic are not reported in this study. Water-saturated experiments can be further confirmed by the presence of free water in the recovered samples. The capsules were loaded into the bottom of the hydrothermal vessel, followed by a filler rod (~6 cm in length) for the vertical vessel, with the purpose of preventing convection. Pressures were generated by

Downloaded from http://pubs.geoscienceworld.org/msa/ammin/article-pdf/108/1/127/5755349/am-2022-8271.pdf
by Institute of Geochemistry Chinese Academy user
on 12 June 2024

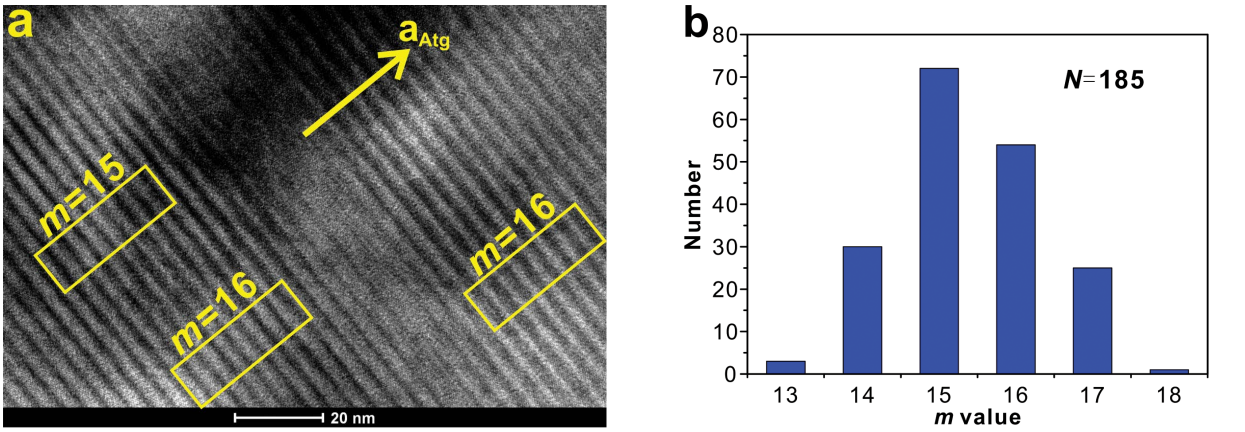

Figure 1. High-resolution TEM image of the starting material (**a**) and histogram of *m* values showing the distribution of periodicities (**b**). (Color online.)

Table 1. Experimental conditions and results for dehydration kinetics of antigorite at a constant pressure of 200 MPa using a Tuttle-type autoclave

Sample no.	*T* (°C)	Duration (h)	Dehydration	Recovered products (wt%)[a]					
				Antigorite	Error[b]	Forsterite	Error	Talc	Error
Atg3	650	18	Yes	0.00	0.00	50.30	(31.10)	49.70	31.08
Atg4	650	3	Yes	41.40	(19.76)	7.60	3.75	51.00	(3.75)
Atg5	650	1	Yes	94.20	(19.78)	1.70	(0.58)	4.10	0.58
Atg7	550	6	No	100.00	0.00	0.00	0.00	0.00	0.00
Atg8	500	240	No	100.00	0.00	0.00	0.00	0.00	0.00
Atg10	650	15	Yes	0.00	0.00	14.20	(5.02)	85.80	(5.02)
Atg11	500	745.5	No	100.00	0.00	0.00	0.00	0.00	0.00
Atg12	650	9	Yes	2.00	(1.96)	18.20	0.78	79.80	(0.79)
Atg21	650	4.5	Yes	4.10	1.93	19.20	(0.62)	76.70	0.62
Atg22	650	6	Yes	3.00	(1.67)	21.20	(2.41)	75.80	2.41
Atg23	650	12	Yes	0.10	(0.10)	55.60	(36.40)	44.30	36.38
Atg26	600	9	Yes	91.00	(2.71)	7.00	(2.86)	3.00	0.00
Atg27	600	15	Yes	81.00	(2.81)	11.00	0.03	8.00	0.00
Atg28	600	36	Yes	39.00	6.41	29.00	4.37	32.00	(7.80)
Atg29	600	48	Yes	54.90	(23.49)	15.60	23.56	29.40	(1.00)
Atg31	600	6	No	100.00	(7.00)	0.00	0.00	0.00	0.00
Atg32	600	24	Yes	79.92	(16.79)	6.70	11.76	13.39	0.00
Atg33	600	60	Yes	21.00	0.04	49.00	(7.50)	30.00	0.10
Atg35	600	84	Yes	17.00	(8.29)	54.00	(11.26)	29.00	2.00
Atg36	650	10.5	Yes	0.00	0.00	46.09	(26.90)	53.91	26.87
Atg41	600	72	Yes	25.00	(11.30)	45.00	(2.81)	30.00	0.60
Atg50	600	120	Yes	26.00	(24.03)	38.00	5.29	37.00	(5.60)
Atg52	650	20	Yes	0.00	0.00	51.49	(32.30)	48.51	32.28
Atg54	580	360	Yes	67.06	4.20	14.91	0.22	18.00	(4.42)
Atg55	565	360	No	100.00	0.00	0.00	0.00	0.00	0.00
Atg57[c]	650	3	Yes	94.70	(2.77)	5.30	(2.10)	0.00	2.10
Atg58[c]	650	6	Yes	86.70	(3.88)	6.30	1.73	7.00	(1.73)
Atg59[c]	650	9	Yes	81.10	(7.18)	8.60	2.82	10.30	(2.82)
Atg60[c]	650	15	Yes	69.70	(11.87)	15.30	3.00	15.00	(3.00)
Atg61[c]	650	48	Yes	14.80	(2.80)	53.30	(1.83)	31.90	1.83
Atg88	625	36	Yes	0.00	0.53	55.10	2.31	44.90	(2.38)
Atg89	625	24	Yes	9.90	(4.76)	51.70	0.03	38.40	(0.09)
Atg90	625	15	Yes	16.40	5.09	50.10	(2.11)	33.50	2.05
Atg91	625	6	Yes	71.10	(5.84)	16.90	(0.31)	11.40	0.89
Atg92	625	3	Yes	82.60	2.45	12.40	(2.41)	5.00	2.40
Atg93	625	1	Yes	95.50	1.08	4.00	(1.42)	0.50	1.41[a]

[a] Uncertainties in quantitative phase analysis may mainly result from the preferred orientation of both antigorite and talc and the grain morphology and size of three phases in the run products.
[b] Error is constrained by the degree of deviation of decomposed antigorite data from the isothermal kinetic curve.
[c] Water-saturated conditions.

pumping water into the vertical vessel and were measured by a pressure gauge with a precision of ±10 MPa (Huang et al. 2017). To monitor temperature, an external K-type thermocouple was inserted into a hole near the bottom of the vessel. Temperature was controlled with an accuracy of ±2 °C. At the end of the experiment, the vessel was chilled by immersion in ice water, thereby decreasing the temperature of gold capsules to <100 °C within a few seconds.

XRD and microstructural observations

After all high *P-T* experiments, the sample powders were recovered from the capsules and then ground for XRD analysis, except for two complementary experiments from which sample powders (Atg103 at 600 °C and initially water-unsaturated conditions for 48 h and Atg112 at 650 °C and water-saturated condi-

Downloaded from http://pubs.geoscienceworld.org/msa/ammin/article-pdf/108/1/127/5755349/am-2022-8271.pdf
by Institute of Geochemistry Chinese Academy user
on 12 June 2024

tions for 3 h) were recovered for microstructural observations under a Zeiss Sigma scanning electron microscopy (SEM) system equipped with an Oxford X-Max 50^N energy-dispersive X-ray spectroscopy (EDS) detector at Guilin University of Technology (Guangxi Province, China). Powder XRD patterns were obtained with a Bruker D8 ADVANCE X-ray diffractometer at both the GIGCAS and IGCEA. The analyses were operated using Cu$K\alpha$ radiation with a 40 kV target voltage and 40 mA target current. Data were collected over the 2θ range of 5–70° with a step of 0.02° and a count time of 19.2 s per step. For the analyses, the powder diffraction files (PDF) cards of antigorite (monoclinic) from Hess et al. (1952), forsterite (orthorhombic) from Hushur et al. (2009), and talc (triclinic) from Rayner and Brown (1973) were employed. For antigorite, the (001) plane at 2θ = 12.114, (002) plane at 2θ = 24.503, (201) plane at 2θ = 35.597, and (211) plane at 2θ = 37.121 were used for comparison with the peaks of the starting material and residual antigorite recovered from the high *P-T* experiments. For forsterite, the (112) plane at 2θ = 36.538, (021) plane at 2θ = 22.898, (130) plane at 2θ = 32.346, (122) plane at 2θ = 39.715, (140) plane at 2θ = 40.096, and (222) plane at 2θ = 52.281 were employed for comparison with the peaks of forsterite formed in the process of antigorite dehydration. For talc, planes (001) and (003) at 2θ = 9.447 and 28.605, respectively, were basically consistent with the peaks of talc in the dehydration products.

Data processing and error evaluation

By calculating the relative area intensities of the strongest diffraction lines in the XRD patterns, subtracting the background, fitting the area intensities of the strongest diffraction peaks with Gaussian curves, and finally normalizing the area intensity to the intensity of the incident beam and acquisition time, we can obtain the transformation degree and relative mass fraction of each solid phase in the experimental product of the antigorite dehydration reaction (e.g., Perrillat et al. 2005). By adding the normalized intensities of the strongest and most obvious diffraction peak areas, a graph of intensity (I) vs. time (t) can be established for each phase. The relative mass fraction or relative intensity is plotted as a function of time to study its effect on the reaction kinetics.

For a dehydration reaction at a given temperature, the degree of departure from the fitted line (with the intercept equivalent to zero) of each data point on the plot of the molar percent of forsterite or talc produced vs. that of antigorite decomposed can be considered the uncertainty. In addition, isothermal kinetic model simulations can be used to provide constraints on the error evaluation of decomposed antigorite. Uncertainties in quantitative phase analysis may mainly result from the preferred orientation of phyllosilicate minerals (i.e., antigorite and talc) and the grain morphology and size of the three phases controlled by kinetic mechanisms.

Results

Reaction progress of antigorite dehydration

Table 1 shows the conditions and results of 36 experiments, in which systematic time-dependent reaction experiments were carried out under the conditions of a confining pressure of 200 MPa and temperatures of 500–650 °C. XRD analysis of all the experimental products showed that only forsterite and talc were produced in our experiments through the following reaction:

$$\text{Antigorite} \rightarrow \text{Forsterite} + \text{Talc} + H_2O. \quad (1)$$

Figure 2 shows a comparison of XRD patterns of dehydrated products over time for representative. From the figure, we can see that there is no substantial dehydration of the antigorite when $t \leq 15$ h; thus, the XRD patterns are basically consistent with that of the starting material. After the phase identification of the experimental products, water subtraction, and normalization of the solid phases, we find that the samples are not dehydrated for durations of 6 h or less and that the degree of dehydration of the sample after 9 h is very small, with only 3 wt% talc produced. The dehydration degree is also small for the 15 h sample, in which the amount of talc produced is only 8 wt% (Table 1). With increasing duration, the characteristic peaks of forsterite and talc in the XRD diffraction pattern are increasingly obvious, and the intensity of the peaks increases. For instance, the amount of talc produced reached 32 wt% in a 36 h sample. We also carried out experiments under a confining pressure of 200 MPa at 580, 565, 550, and 500 °C (Table 1). The maximum durations for operation under these target *P-T* conditions were 360, 360, 6, and 745.5 h, respectively. The results show that dehydration of antigorite does not occur at 565 °C but occurs significantly at 580 °C, suggesting that a temperature between 565 and 580 °C can be regarded as the temperature stability limit of antigorite under 200 MPa pressure.

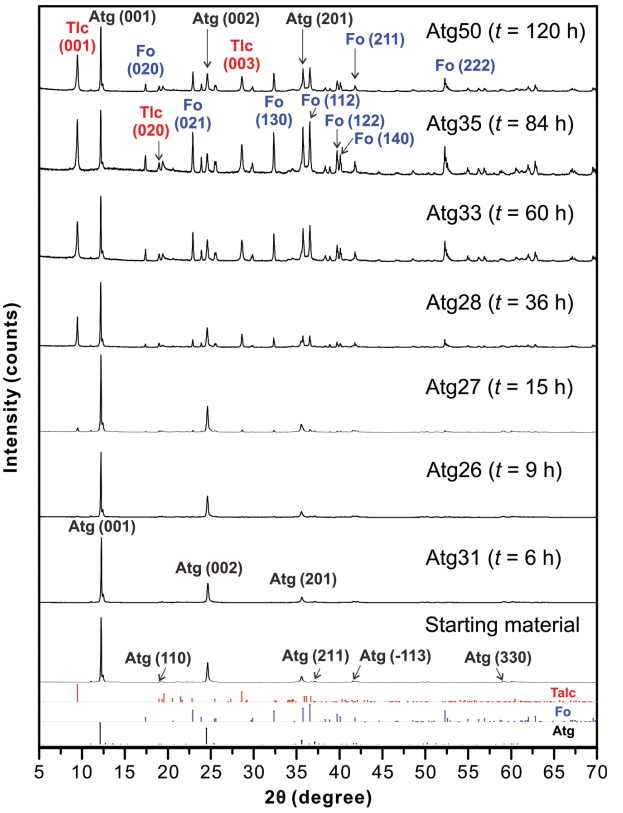

Figure 2. Comparison of XRD patterns of experimental products over time for representative samples under the initially water-unsaturated conditions of 200 MPa confining pressure and 600 °C temperature. Below the graph are the XRD lines of talc (Rayner and Brown 1973), forsterite (Hushur et al. 2009), and antigorite (Hess et al. 1952). Atg = antigorite; Fo = forsterite; Tlc = talc. (Color online.)

As clearly shown in Figure 3, with increasing duration, the decomposition of antigorite increases rapidly at first and then slowly; correspondingly, the production of talc and forsterite exhibits similar changes. However, the degrees of decomposition of antigorite and crystallization of talc and forsterite are distinct. Under initially water-unsaturated conditions, the degrees of change in the three phases are more obvious for experiments at 625 and 650 °C (Figs. 3b and 3c). Furthermore, the reaction rate at 650 °C is much faster than that at 625 °C, and the reaction rate at 625 °C is much faster than that at 600 °C. Accordingly, at 650 °C, the decomposition of antigorite and the crystallization of both forsterite and talc reach near completion within 9 h. In contrast, the reaction

Downloaded from http://pubs.geoscienceworld.org/msa/ammin/article-pdf/108/1/127/5755349/am-2022-8271.pdf
by Institute of Geochemistry Chinese Academy user
on 12 June 2024

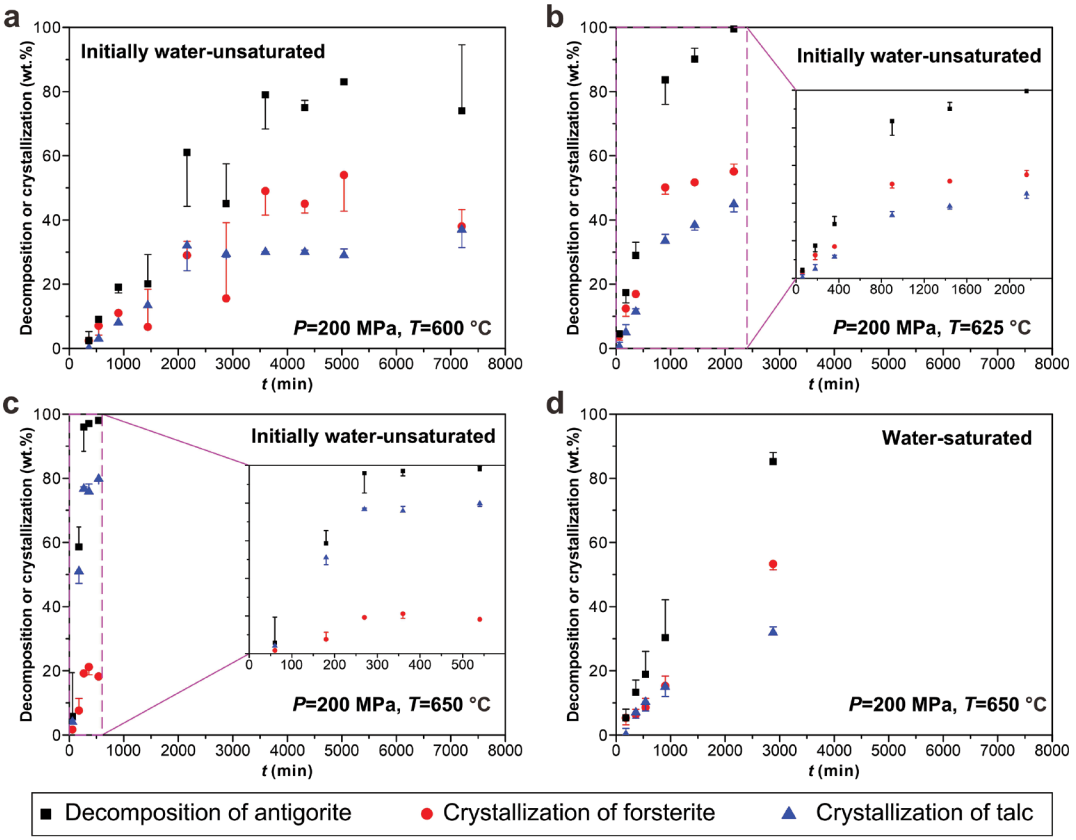

Figure 3. Variations in decomposition of antigorite and crystallization of forsterite and talc (wt%) with time (min) for the dehydration reaction of antigorite to forsterite + talc at 600 (**a**), 625 (**b**), and 650 °C (**c** and **d**). Panels **a**–**c** display data under initially water-unsaturated conditions, while panel **d** shows data under water-saturated conditions. Vertical line represents error. (Color online.)

progress at 600 °C is ~80% when the duration is up to 84 h and changes very slowly thereafter (Fig. 3a), implying that the water activity is close to 1 (i.e., water saturation) beginning at 84 h. The data point scattering reflects the uncertainty in the quantitative phase analysis. Under water-saturated conditions, however, the reaction rate is much slower at 650 °C (Fig. 3d).

Kinetic parameters

In our experiments, antigorite dehydrates to only forsterite + talc + water, and the Avrami model suitable for heterogeneous solid-state reactions (Avrami 1939) is thus used to simulate the isothermal kinetic data of the experimental products over time at 600, 625, and 650 °C. To study the dehydration kinetics, the strongest peak area calculation is performed for all XRD measurements on recovered run products. For instance, for the strongest peak of antigorite, the peak area at a given temperature before the start of the reaction is regarded as the initial intensity I_0, and the intensity at time t for a given P-T condition is marked as I_t; then, I_t/I_0 represents the relative intensity. For isothermal reactions, the reaction progress α can be expressed as follows:

$$\alpha = 1 - I_t/I_0. \quad (2)$$

where I_t represents the integrated intensity of a peak at time t (e.g., Wang et al. 2015). This reaction progress can be well described by the classic Avrami model, which includes the two processes of nucleation and growth and can be expressed by the following equation:

$$\alpha = 1 - \exp(-kt^n). \quad (3)$$

where t is the time in seconds, k is the rate constant, and n is the Avrami exponent. As the Avrami constants, the parameters k and n are considered to indicate the nucleation and crystallization mechanisms. In terms of a combination of nucleation and growth processes, Cahn (1956) derived the theoretical n value in the Avrami equation, which varies from 1 to 4. The k and n values are considered to depend on both the time and dimensionality or morphology of the nucleation and growth processes. For $n = 1$, the nucleation rate is faster than the growth rate, and when $n = 4$, the growth rate is faster than the nucleation rate.

Figure 4 shows the fitting to the experimental data at 600, 625, and 650 °C, and the results are summarized in Table 2. Fitting of the data under initially water-unsaturated conditions yields $n = 1.33 \pm 0.13$ and $\ln k = -15.92 \pm 1.49$ at 600 °C, $n = 1.40 \pm 0.02$ and $\ln k = -14.83 \pm 0.38$ at 625 °C, and $n = 1.50 \pm 0.02$ and $\ln k = -13.50 \pm 0.38$ at 650 °C for the decomposition of antigorite (Fig. 4a); $n = 1.37 \pm 0.08$ and $\ln k = -15.84 \pm 0.90$ at 600 °C, $n = 1.24 \pm 0.01$ and $\ln k = -13.21 \pm 0.19$ at 625 °C, and $n = 1.15 \pm 0.01$ and $\ln k = -11.19 \pm 1.67$ at 650 °C for the crystallization of forsterite (Fig. 4b);

Downloaded from http://pubs.geoscienceworld.org/msa/ammin/article-pdf/108/1/127/5755349/am-2022-8271.pdf
by Institute of Geochemistry Chinese Academy user
on 12 June 2024

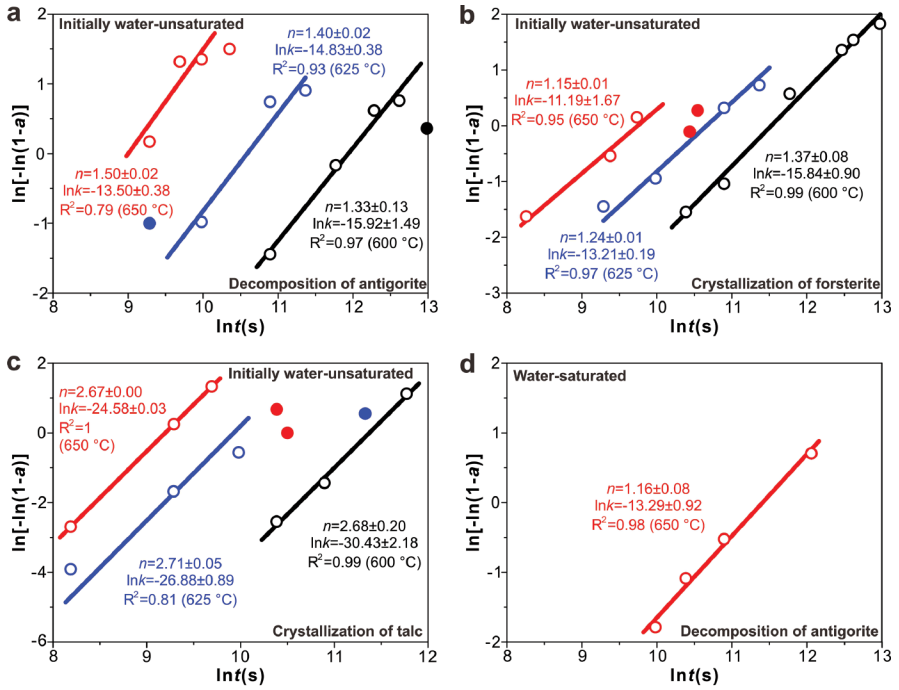

Figure 4. Plots of ln[–ln(1–α)] vs. ln(t) for each solid phase involved in reaction 1 at 600, 625, and 650 °C. Decomposition of antigorite (**a** and **d**) and crystallization of forsterite (**b**) and talc (**c**) occur in reaction 1. Reactions shown in panels **a**–**c** are under initially water-unsaturated conditions, while those shown in panel **d** are under water-saturated conditions. The slopes of the lines fit to the data points marked by hollow circles represent the n values that best describe the reaction mechanisms. Data points marked by solid circles have not been included for the fitting due to large errors. (Color online.)

Table 2. Information on kinetic mechanism parameters for dehydration of antigorite and crystallization of forsterite and talc

Phase	T (°C)	n	ln$k$	R^2
Antigorite	600	1.33 ± 0.13	−15.92 ± 1.49	0.97
	625	1.40 ± 0.02	−14.83 ± 0.38	0.93
	650	1.50 ± 0.02	−13.50 ± 0.38	0.79
	650[a]	1.16 ± 0.08	−13.29 ± 0.92	0.98
Forsterite	600	1.37 ± 0.08	−15.84 ± 0.90	0.99
	625	1.24 ± 0.01	−13.21 ± 0.19	0.97
	650	1.15 ± 0.18	−11.19 ± 1.67	0.95
Talc	600	2.68 ± 0.20	−30.43 ± 2.18	0.99
	625	2.71 ± 0.05	−26.88 ± 0.89	0.81
	650	2.67 ± 0.00	−24.58 ± 0.03	1.00

[a] Water-saturated conditions.

and $n = 2.68 \pm 0.20$ and ln$k = -30.43 \pm 2.18$ at 600 °C, $n = 2.71 \pm 0.05$ and ln$k = -26.88 \pm 0.89$ at 625 °C, and $n = 2.67 \pm 0.00$ and ln$k = -24.58 \pm 0.03$ at 650 °C for the crystallization of talc (Fig. 4c). Under water-saturated conditions, $n = 1.16 \pm 0.08$ and ln$k = -13.29 \pm 0.92$ at 650 °C for the decomposition of antigorite (Fig. 4d).

The reaction rate constant k shown in Equation 3 is expressed by the Arrhenius equation:

$$k = A\exp(-E/RT) \quad (4)$$

where A is the pre-exponential factor, E is the activation energy in kJ/mol, R is the gas constant (8.314 J K/mol), and T is the absolute temperature in degrees Kelvin. The fitted line shown in Figure 5 can be obtained by plotting the natural logarithm of the rate constant and the reciprocal of the absolute temperature, which gives the value of E as 353.5 ± 23.7 kJ/mol. Uncertainty on activation energy is calculated from the uncertainty of the slope of the line fit to the data points and does not include propagated errors from the uncertainty on each data point.

Discussion

The activation energy value obtained in the present study is higher than the two average activation energies (268.1 and 299.2 kJ/mol) obtained by Liu et al. (2019) based on the double Gaussian distribution activation energy model (2-DAEM), but lower than the value (400 kJ/mol) obtained by the same authors using the Flynn-Wall-Ozawa model (Table 3). Furthermore, it is also higher than the activation energy reported by Sawai et al. (2013) and Gualtieri et al. (2012); but lower than the activation energy given by Weber and Greer (1965) (Table 3). However, Gualtieri et al. (2012) concluded that the activation energy of their sample was much lower than that reported by Weber and Greer (1965) because their sample consisted of only ~79 wt% antigorite. They speculated that if ~21 wt% of impurities, i.e., chrysotile, which is one of the main low-temperature serpentine minerals, were removed, the activation energy of the sample consisting of 100% antigorite would be ~322 kJ/mol (Gualtieri et al. 2012), which is very close to the value of 353.5 ± 23.7 kJ/mol that we obtained for the nearly pure antigorite sample. As the pre-exponential factor is linearly correlated with the activation energy, the difference in activation energy may result from a large change in the absolute value of the activation energy caused by the pre-exponential factor (Liu et al. 2019). According to Equation 4, this difference in activation energy can be used to

Downloaded from http://pubs.geoscienceworld.org/msa/ammin/article-pdf/108/1/127/5755349/am-2022-8271.pdf
by Institute of Geochemistry Chinese Academy user
on 12 June 2024

reflect the change in the reaction rate (kinetic). Thus, the factors (such as particle size, modulation structure, etc.) affecting dehydration kinetics can be considered to have an effect on the activation energy. In addition, chemical and structural differences in the starting material of antigorite (Wunder et al. 1997, 2001) and water activity (Perrillat et al. 2005) may possibly result in slightly different *P-T* locations and invariant points for the serpentine dehydration reaction (e.g., Ulmer and Trommsdorff 1995; Wunder and Schreyer 1997; Fig. 6).

Factors influencing the dehydration kinetics and phase stability

Several high *P-T* experimental studies (Bose and Ganguly 1995; Bromiley and Pawley 2003; Ulmer and Trommsdorff 1995; Wunder and Schreyer 1997) and field observations of eclogite-facies rocks (Auzende et al. 2002; Guillot et al. 2000; Scambelluri et al. 1995) have shown that antigorite is the only serpentine variety that can exist stably under mantle conditions. Additionally, antigorite follows reaction 1 at high temperatures of 600–700 °C and pressures lower than ~2 GPa (Fig. 6; Ulmer and Trommsdorff 1995). Our experiments were performed at a constant pressure of 200 MPa, and the XRD analyses of the products indicated that only forsterite and talc were produced in addition to water, which is consistent with the results of previous studies (e.g., Evans et al. 1976; Ulmer and Trommsdorff 1995; Wunder and Schreyer 1997; Fig. 6). As illustrated in Figure 6, our data show that the dehydration temperature (~570 °C) of our antigorite (m = 15) is slightly higher than the reaction boundaries (~540 ± 10 °C) at 200 MPa based on the data of Evans et al. (1976) and Wunder and Schreyer (1997), which may be due to the lower m value of our samples than theirs (m = 17). This is also one of the reasons that our sample has a higher stability and activation energy than the antigorite used in previous dehydration kinetics studies (e.g., Liu et al. 2019; Sawai et al. 2013) (Table 3), because for dehydration at the same temperature, a

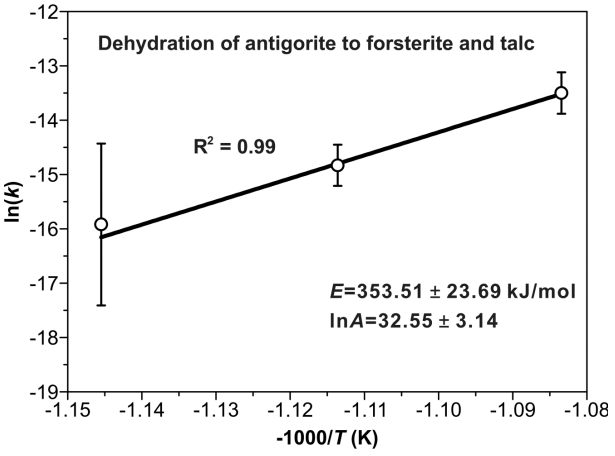

Figure 5. Arrhenius diagram of the dehydration of antigorite. As shown in this figure, the activation energy, E, can be calculated from the slope of the solid line.

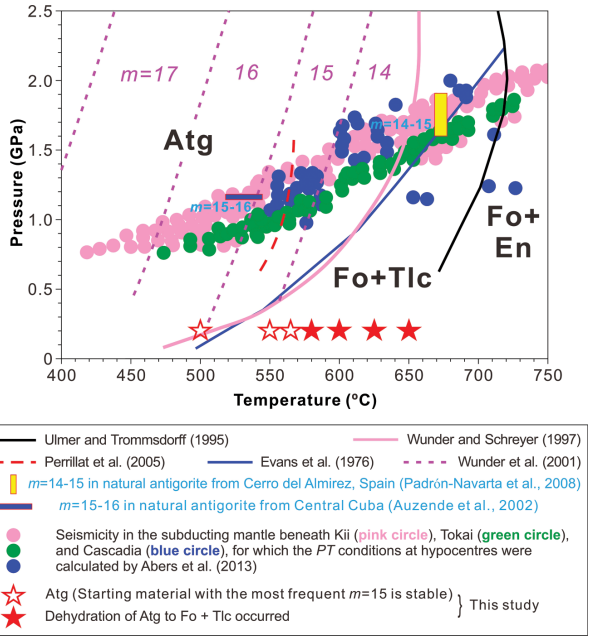

Figure 6. *P-T* conditions of the present experiments (red stars) and a MgO-SiO_2-H_2O (MSH) phase diagram constructed with a blue line, black line, pink line, and red dashed line representing the phase boundaries defined by the data of Evans et al. (1976), Ulmer and Trommsdorff (1995), Wunder and Schreyer (1997), and Perrillat et al. (2005), respectively. The phase boundary represented by the red dashed line corresponds to low-water activity. Magenta dotted lines delimit *P-T* ranges for different m-isolines of synthetic antigorite, which are labelled by magenta italic numbers, in the MSH system determined by Wunder et al. (2001). The yellow vertical bar with m = 14–15 represents natural antigorite from Cerro del Almirez, Spain (Padrón-Navarta et al. 2008). The blue horizontal bar with m = 15–16 is shown for natural antigorite from central Cuba (Auzende et al. 2002). Circles show the *P-T* conditions at hypocenters calculated by Abers et al. (2013) for seismicity in the subducting mantle beneath southwestern Japan [Kii (pink circle), Tokai (green circle)] and Cascadia (blue circle). Hollow stars indicate the starting material (i.e., antigorite) with the most frequently observed m = 15 (Fig. 1), which is stable and undecomposed under the corresponding *P-T* conditions, and solid stars indicate the occurrence of dehydration of the starting material to produce forsterite + talc under the corresponding *P-T* conditions. Atg = antigorite; Fo = forsterite; Tlc = talc; En = enstatite. (Color online.)

Table 3. Activation energies of the dehydration of antigorite from the literature

Activation energy (kJ/mol)	Comment	Methods	References
268.1	slow dehydration	thermogravimetric analysis and 2-DAEM	Liu et al. (2019)
299.2	fast dehydration		
400		thermogravimetric analysis and Flynn-Wall-Ozawa	
219	water band 1	in situ high-temperature infrared spectroscopy	Sawai et al. (2013)
243	water band 2		
256	water band 3		
255	612–708 °C	in situ powder XRD and TEM	Gualtieri et al. (2012)
444–728	689–766 °C	thermogravimetric analysis and XRD	Weber and Greer (1965)

Downloaded from http://pubs.geoscienceworld.org/msa/ammin/article-pdf/108/1/127/5755349/am-2022-8271.pdf
by Institute of Geochemistry Chinese Academy user
on 12 June 2024

lower equilibrium dehydration temperature boundary (higher *m* value) will result in a faster reaction rate and a corresponding lower activation energy. For similar *m* values, the dehydration temperature of our sample and that of a natural sample from Cerro del Almirez, Spain (Padrón-Navarta et al. 2008), at different pressures can be used to delineate a reaction boundary, which has a trend similar to the reaction boundaries determined by Evans et al. (1976) and Wunder and Schreyer (1997).

Previous studies suggested that if the system contains a small amount of aluminum, the entire phase boundary will migrate to a higher temperature by ~50–100 °C (e.g., Bromiley and Pawley 2003). However, our antigorite contains only 0.06 wt% Al_2O_3, which is much lower than the aluminum contents of the samples used previously [e.g., 3.45 wt% in Perrillat et al. (2005) and Chollet et al. (2011); 1.51 wt% in Inoue et al. (2009); 1.73 wt% in Sawai et al. (2013); and 1.03 wt% in Liu et al. (2019)]. In contrast, the effect of iron on the thermal stability of antigorite is twofold. On the one hand, Fe^{2+} is known to reduce its stability by ~15–20 °C (Ulmer and Trommsdorff 1999); on the other hand, Fe^{3+}, like Al and Cr, could stabilize antigorite to higher *P-T* conditions (e.g., Bromiley and Pawley 2003; Debret et al. 2015; Padrón-Navarta et al. 2008, 2013). Recently, 10 wt% FeO was determined to decrease the stability of antigorite by only 25 °C (Merkulova et al. 2016), suggesting that the effect of iron is subordinate to that of Al. The amount of iron contained in our sample is 0.97 wt% TFeO; thus, the effect of low iron and aluminum contents on the phase boundary of antigorite might be partially offset.

The sample powders used in this study (~10–15 μm) are slightly larger than those in some previous experiments [e.g., 5–10 μm in Liu et al. (2019) and 2–3 μm in Perrillat et al. (2005)]. This may be not only another reason why our sample dehydration temperature is slightly higher than theirs within a certain time frame (e.g., Llana-Fúnez et al. 2007) but also one of the main reasons for the higher activation energy of our coarse-grained samples than those of the fine-grained samples used in previous studies (Liu et al. 2019; Perrillat et al. 2005) (Table 3). The effect of grain size on dehydration kinetics can also be reflected by the differences in activation energy of various grain sizes, as the lower the activation energy is, the faster the reaction rate is. For example, earlier experiments on the dehydration kinetics of trehalose dihydrate performed by Taylor and York (1998) suggested that the activation energy decreases with decreasing particle size because smaller particles contain more lattice defects, allowing water to be released more easily, and thus have lower activation energy. Similar results were also reflected in the study of lizardite dehydration kinetics by Llana-Fúnez et al. (2007), who determined average activation energies of 429 ± 201 and 528 ± 34 kJ/mol for powdered and intact samples, respectively. Correspondingly, the dehydration rate of powdered samples is 10 times faster than that of intact samples under the same conditions (Llana-Fúnez et al. 2007). Concurrently, Candela et al. (2007) studied the dehydration kinetics of chrysotile at low pressure and found that fine particles with large surface-to-volume ratios dehydrated more rapidly than larger particles. In this regard, the dehydration kinetics of antigorite were proposed to be dominated by the diffusion of hydrogen in the mineral. If this is correct, the kinetics could be a function of the diffusion length of hydrogen, which is proportional to the specific surface of the grains or the square of the inverse of the grain size (Sawai et al. 2013). Thus, doubling the grain size results in four-times slower kinetics. In addition, the diffusion coefficient of hydrogen in the mineral should depend on temperature, probably with an Arrhenius relation, and thus may be a source of the temperature dependence of the dehydration kinetics of antigorite (Sawai et al. 2013). Wang et al. (2015) conducted an experimental study on the dehydration kinetics of natural talc and found that the dehydration rate of talc increased with decreasing particle size, but when the particle size was <5 μm, there was almost no effect on the dehydration rate. Therefore, fine-grained antigorite is generally more likely to dehydrate, and the dehydration rate may be faster than that of a coarse-grained sample.

In addition, water activity is an important factor affecting the dehydration boundary of antigorite. Previous studies have shown that the stability limit of antigorite (i.e., the highest temperature under water-saturated conditions) shifts toward lower temperatures with decreasing water activity (e.g., Perrillat et al. 2005; Hilairet et al. 2006; Fig. 6). As shown in Table 1 and Figure 3d, the water-saturated samples (Atg60 and Atg61) do not completely decompose to form forsterite + talc at long durations, but the initially water-unsaturated sample Atg23 under the same *P-T* conditions does nearly completely decompose. The powdered samples Atg60 and Atg61 are immersed in water so that the voids within the sample powders are filled with water to form a water-saturated environment, which is supported by the presence of free water in the recovered sample (e.g., Perrillat et al. 2005). In contrast, the voids within sample Atg23 are partially filled with water generated only by the decomposition of the sample itself, the water activity of the sample increases with duration, and the sample becomes water saturated until near completion of the dehydration reaction. Furthermore, we find that the rate of dehydration slows down significantly when the sample is heated at 600 °C for 60–120 h (Fig. 3a), which means that the water activity of the sample increases, making it impossible for our antigorite to completely dehydrate at this temperature. At higher temperatures (625 and 650 °C), however, the rate of dehydration decreases significantly when the sample is nearly completely decomposed in much shorter durations (Figs. 3b and 3d). This response implies that an increase in temperature can offset the effect of an increase in water activity.

In summary, combining our results with those of previous studies, the stability of antigorite is affected by the modulation structure (i.e., *m* value), aluminum content, iron content, water activity, and deformation within the Earth. Antigorites with low-*m* values can be stabilized at higher temperatures. An increase in aluminum or Fe^{3+} content can cause the stable boundary to move toward higher temperatures, while an increase in Fe^{2+} content has the opposite and smaller effect. Water activity acts as the driver of the reaction and determines the stability of the antigorite under certain *P-T* conditions (e.g., Perrillat et al. 2005). Different from our static experiments, differential stress must be present within the earth where deformation geometry (such as compression, shear, or the direction of the foliation plane with respect to the maximum principal stress) may change the phase stability of antigorite and thus its dehydration kinetics (Okazaki and Katayama 2015; Shao et al. 2021, 2022; Takahashi et al. 2011). A reduction

Downloaded from http://pubs.geoscienceworld.org/msa/ammin/article-pdf/108/1/127/5755349/am-2022-8271.pdf
by Institute of Geochemistry Chinese Academy user
on 12 June 2024

in particle size can increase the reaction rate (Candela et al. 2007; Llana-Fúnez et al. 2007; Taylor and York 1998).

Kinetic mechanism

For the decomposition of antigorite, higher n values are found at high temperatures than at low temperatures (Fig. 4; Table 2). The mean n value for antigorite decomposition at the three experimental temperatures is 1.41 ± 0.09, indicating an instantaneous nucleation mechanism followed by a growth process governed by chemical species diffusing to the crystal surface (Christian 1975). Such a mechanism was reported by Perrillat et al. (2005) for the crystallization of forsterite and talc-like phases in the process of antigorite dehydration. The n value (n = 1.37) for the crystallization of forsterite is close to that (n = 1.33) for the decomposition of antigorite at 600 °C in the same reaction process. However, the value of n for the crystallization of forsterite decreases to 1.15 when the temperature increases to 650 °C (Fig. 4), indicating that the crystallization of forsterite is mainly controlled by the growth process with increasing temperature and is accompanied by rapid nucleation saturation. In contrast, the crystallization of talc shows little change in the n value at 600, 625, and 650 °C (average n = 2.69 ± 0.02), suggesting that the formation mechanism of talc is the same at the three temperatures and is dominated by nucleation. In other words, the nucleation rate of forsterite becomes quite high with increasing temperature, while at the initial stage of the reaction, the nucleation of talc is not instantaneous but slow and then increases with time. In addition, the k values of the three minerals increase with increasing temperature, which is similar to the results of a study on talc dehydration kinetics (Wang et al. 2015). Using various methods, however, previous studies determined different kinetic mechanisms for antigorite dehydration. Based on XRD, for example, Perrillat et al. (2005) obtained n = 2 for the dehydration of antigorite, indicating a mechanism of surface growth at the grain edge. In contrast, also using XRD, Gualtieri et al. (2012) found that antigorite dehydration is controlled by a one-dimensional diffusion process, which is similar to the finding obtained by Sawai et al. (2013) using in situ high-temperature infrared spectroscopy analysis. In terms of thermogravimetric analysis and in situ XRD, Balucan et al. (2011) found that the dehydration kinetics of antigorite can be well modeled by a three-dimensional phase boundary reaction model. Most recently, also employing thermogravimetric analysis, Liu et al. (2019) determined that the antigorite dehydration kinetics follow 2-DAEM. However, most of these studies did not perform microstructural observations of products to support their analyses of the kinetic mechanism of antigorite dehydration.

To confirm our kinetic results, we conducted two complementary experiments (Atg103 and Atg112) and further analysis of the run products. Figure 7 shows backscattered electron (BSE) images of the recovered products produced at 600 and 650 °C. Under 600 °C and initially water-unsaturated conditions, the experiment conducted for 48 h generated abundant fine grains of forsterite (Fig. 7a), suggesting that the formation of forsterite is controlled by the growth process, followed by rapid nucleation saturation. Furthermore, large crystals of talc were generated in this experiment, indicating that the formation of talc is mainly controlled by nucleation. These observations based on the BSE images of the recovered samples were consistent with the kinetic

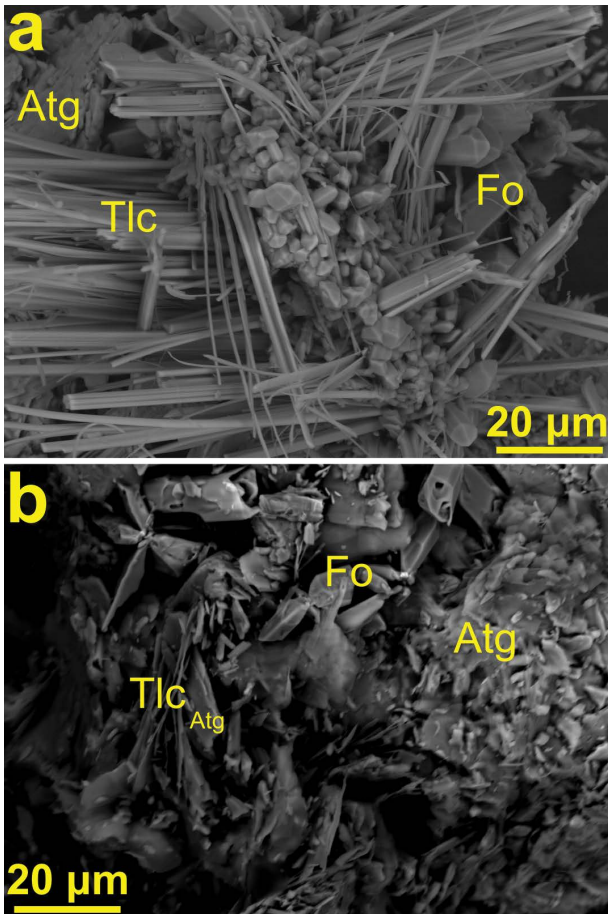

Figure 7. BSE images of recovered run products. (**a**) Atg103 under 600 °C and initially water-unsaturated conditions for 48 h. (**b**) Atg112 under 650 °C and water-saturated conditions for 3 h. (Color online.)

results that n = ~1.3 for the formation of forsterite and ~2.7 for the formation of talc. Under 650 °C and water-saturated conditions, in contrast, the amounts of forsterite and talc produced were much lower in the experiment conducted for only 3 h (Fig. 7b), which is basically consistent with the results of the powder XRD analyses.

Isothermal kinetic model and fluid production rates

Previous studies have shown that the hypocenters of the lower-plane seismicity in a DSZ are roughly distributed along the estimated location of the 600–650 °C isotherms (e.g., Peacock 2001). According to the abovementioned dehydration kinetics of antigorite at 600 and 650 °C, we can calculate the fluid production rate during the antigorite dehydration process at the two end-member temperatures corresponding to the isotherms bounding the hypocenters. On the basis of the fitting to the decomposition of antigorite at the two temperatures, as shown in Figures 4a and 4d, we obtain the following relationships indicating the variation in the progress of the dehydration reaction with time at 600 and 650 °C:

$$\alpha(T = 600\ ^{\circ}\mathrm{C}\ \text{and initially water-unsaturated}) = 1 - \exp\left(-\frac{t^{1.33\pm0.13}}{8178342.01\pm0.23}\right) \quad (5)$$

Downloaded from http://pubs.geoscienceworld.org/msa/ammin/article-pdf/108/1/127/5755349/am-2022-8271.pdf
by Institute of Geochemistry Chinese Academy user
on 12 June 2024

$$\alpha(T = 650\ ^\circ\text{C and initially water-unsaturated}) = 1 - \exp\left(-\frac{t^{1.50\pm0.02}}{716404.33 \pm 0.68}\right) \quad (6)$$

$$\alpha(T = 650\ ^\circ\text{C and water-saturated}) = 1 - \exp\left(-\frac{t^{1.16\pm0.08}}{588893.13 \pm 0.40}\right) \quad (7)$$

Figure 8 shows the curves indicating variations in the progress of the reaction with time at 600 and 650 °C calculated according to the above three equations. Some data points at 600 °C seriously depart from the curve because these data have large errors and thus were not included in fitting to obtain n and k used for modeling the curve. Despite the large errors of some data points, most of the data are consistent with the simulated dehydration kinetics curve. The rate of antigorite dehydration clearly increases with increasing temperature under initially water-unsaturated conditions. At t = 800 min, for instance, the antigorite dehydration progress is only ~18.96% at 600 °C and almost 100% at 650 °C under initially water-unsaturated conditions, while it is only ~37.96% at 650 °C under water-saturated conditions. When half of the antigorite is consumed during the breakdown reaction, the dehydration rate can be obtained according to the half-life of the reaction (e.g., Chollet et al. 2011)

$$V_{1/2} = \frac{C_{H_2O}}{t_{1/2}} \times \frac{\rho}{\rho_{H_2O}} \quad (8)$$

where $t_{1/2}$ is the half-life of the reaction when the reaction progress is 50% and C_{H_2O} represents the water content of the mineral. ρ and ρ_{H_2O} are the densities of the mineral and water, respectively. In this study, antigorite has a density of 2.593 g/cm^3 and a water content of ~12.19 wt%. At a pressure of 1.5 GPa, the water density is ~1.057, ~1.048, and ~1.038 g/cm^3 at 600, 625, and 650 °C, respectively (Zhang and Duan 2005). As shown in Figure 8, the half-lives of the antigorite dehydration reaction at 600, 625, and 650 °C under initially water-unsaturated conditions are 32.65, 8.48, and 1.77 h, respectively. In contrast, the half-life of antigorite breakdown at 650 °C under water-saturated conditions is 18.37 h. Therefore, the calculated fluid production rates in the process of antigorite dehydration at 600, 625, and 650 °C under initially water-unsaturated conditions are 2.54×10^{-6}, 9.80×10^{-6}, and 4.69×10^{-5} $m^3_{fluid}m^{-3}_{rock}s^{-1}$, respectively. Under initially water-saturated conditions, the calculated fluid production rate is 4.52×10^{-6} $m^3_{fluid}m^{-3}_{rock}s^{-1}$ at 650 °C, which is ~10 times slower than that under initially water-unsaturated conditions at the same temperature, similar to the result of Perrillat et al. (2005). These values are comparable to those reported previously for antigorite dehydration (3×10^{-5} to 3×10^{-4} $m^3_{fluid}m^{-3}_{rock}s^{-1}$ at 625–700 °C in Sawai et al. (2013), 8×10^{-5} $m^3_{fluid}m^{-3}_{rock}s^{-1}$ at 620 °C, and 4.4×10^{-4} $m^3_{fluid}m^{-3}_{rock}s^{-1}$ at 660 °C in Liu et al. (2019), 10^{-4} $m^3_{fluid}m^{-3}_{rock}s^{-1}$ in Chollet et al. (2011), and 3×10^{-8} to 3×10^{-6} $m^3_{fluid}m^{-3}_{rock}s^{-1}$ in Perrillat et al. (2005)). Likewise, the rate at which antigorite dehydration releases fluids in this study is far greater than the viscous relaxation rate of antigorite (3.0×10^{-12} to 3.0×10^{-7} s^{-1}, i.e., the reciprocal of Maxwell's relaxation time) under subduction zone conditions reported by Hilairet et al. (2007). Previous studies have shown that pressure has no obvious effect on the dehydration kinetics of antigorite (e.g., Perrillat et al. 2005; Rubie and Thompson 1985). Thus, the fluid production rate calculated above can be applied to shallow intermediate-depth earthquake layers in hot subduction zones (e.g., Kii, Tokai, and Cascadia), where antigorite breakdown into forsterite + talc + water is possible (Fig. 6).

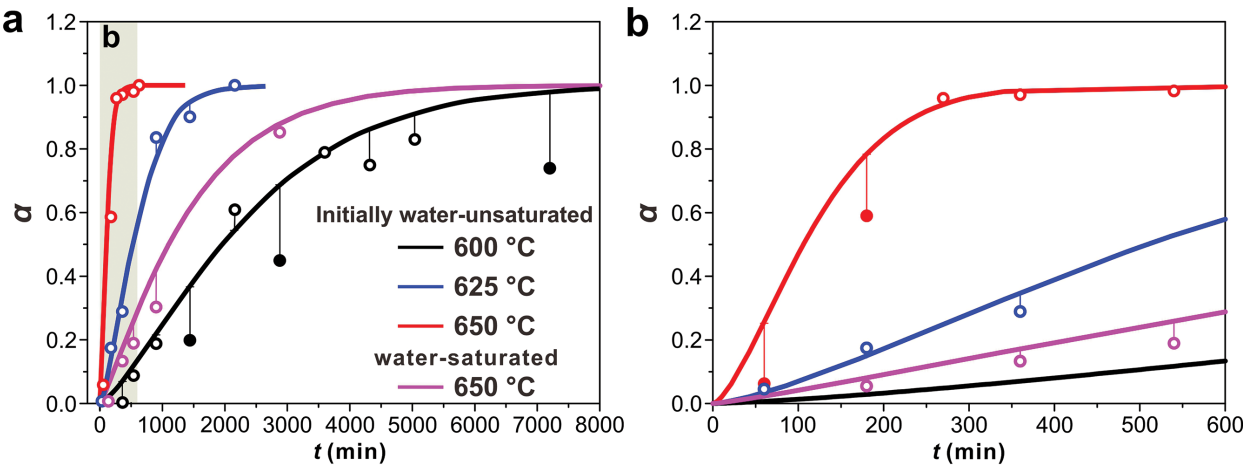

Figure 8. Dehydration kinetic models for antigorite at 600 and 650 °C, corresponding to the end-member isotherms bounding the hypocenters of the lower-plane seismicity of a DSZ, derived from the parameters of isothermal experiments. Models for antigorite dehydration kinetics at 625 °C and initially water-unsaturated conditions and at 650 °C and water-saturated conditions are also included for comparisons. A solid line represents an initially water-unsaturated model, while a dashed line shows a water-saturated model. The hollow circles represent the experimental data used for fitting n and k that are used to stimulate the kinetic curves, while the data marked by solid circles are not included for fitting. Vertical line represents the degree of deviation of data from the curve, which can be used to constrain the error of the data. Panel **b** is the close-up of 0–600 min in panel **a**. (Color online.)

Downloaded from http://pubs.geoscienceworld.org/msa/ammin/article-pdf/108/1/127/5755349/am-2022-8271.pdf
by Institute of Geochemistry Chinese Academy user
on 12 June 2024

Implications

For decades, intermediate-depth earthquakes have commonly been considered to result from the dehydration of antigorite (e.g., Chollet et al. 2011; Ferrand et al. 2017; Hilairet et al. 2006; Liu et al. 2019; Miller et al. 2003; Raleigh and Paterson 1965; Reynard 2013; Sawai et al. 2013). In their pioneering work on dehydration embrittlement, Raleigh and Paterson (1965) deformed natural serpentinites, which contained other phases, such as olivine, and explained that embrittlement occurred within the dehydrating antigorite due to fluid overpressure. However, many later experiments have indicated that embrittlement occurs in adjacent more brittle peridotite or the piston rather than in the dehydrating antigorite itself (e.g., Dobson et al. 2002; Ferrand et al. 2017; Jung et al. 2004; Xia 2013). In fact, antigorite shows semi-brittle behavior under mantle conditions, and no dehydration embrittlement occurs (e.g., Chernak and Hirth 2011; Gasc et al. 2011; Shao et al. 2021). In the lithospheric mantle, only partial serpentinization (17–31%) occurs (Garth and Rietbrock 2014), and the distribution of serpentine is heterogeneous (Dunkel et al. 2017). Some researchers have proposed that the fluid produced by antigorite dehydration at intermediate depths in a subduction zone likely migrates into the surrounding brittle peridotite region (Barcheck et al. 2012; Rutter et al. 2009) to generate not only high pore fluid pressure but also instantaneous over stress due to the lateral transfer of the stress previously supported by the dehydrating antigorite, thereby inducing earthquakes. This inference is partially similar to the sudden stress transfer model proposed by Ferrand et al. (2017), but it is probably true at $P < 2$ GPa, whether or not the embrittlement of peridotite around the dehydrating antigorite occurs was considered to depend on the competition between the rate of fluid production and migration into the peridotite and the deformation rate of the peridotite (e.g., Chollet et al. 2011; Liu et al. 2019; Perrillat et al. 2005). In the case when fluid migration from dehydrating antigorite to adjacent peridotite is negligible, if fluid is produced at a faster rate than deformation, a seismic rupture may be nucleated. However, several studies have shown that fast dehydration kinetics may not lead to dehydration embrittlement (e.g., Chernak and Hirth 2011; Gasc et al. 2011).

Under the conditions of a syndeformational antigorite dehydration reaction, there must be another heterogeneous system, namely, antigorite and its dehydration products (e.g., Takahashi et al. 2011). As stated by Gasc et al. (2011), we should emphasize the role of reaction products whose grain size is in turn controlled by reaction kinetics (Rutter and Brodie 1988). In a recent study by Proctor and Hirth (2015), forsterite produced by the dehydration of antigorite has a finer grain size in drained samples than in undrained samples. This means that in the interior of the Earth, the dehydration of antigorite may produce finer-grained forsterite (<1 μm) than that observed in our undrained experiments (Fig. 7). Such fine-grained forsterites may facilitate faulting by their superplasticity (Rutter and Brodie 1988; Schubnel et al. 2013). However, several studies suggest that stick-slip occurs under conditions where dehydration of antigorite happens (Okazaki and Katayama 2015; Shao et al. 2022; Takahashi et al. 2011). SEM observations also indicate heterogeneous dehydration products (Takahashi et al. 2011), in which forsterite displays velocity weakening (Boettcher et al. 2007; King and Marone 2012) while antigorite shows velocity strengthening and thus inhibits normal stick-slip behavior (Chernak and Hirth 2011; Shao et al. 2021). Consequently, when significant dehydration occurs in the core of a serpentinized fault zone at 650 °C, normal stick-slip behavior can be expected as the velocity-weakening behavior of forsterite dominates the frictional properties of the entire fault gouge (Boettcher et al. 2007; King and Marone 2012; Okazaki and Katayama 2015). Once triggered, an earthquake will propagate into the more brittle surrounding rocks. At 600 °C, slow stick-slip could be induced by the interaction between the velocity strengthening behavior of antigorite and the velocity-weakening behavior of forsterite (Okazaki and Katayama 2015). In addition, unstable slip can also be induced by water or talc because such phases may reduce the rate dependence of antigorite (e.g., Moore and Lockner 2011; Okazaki and Katayama 2015), thereby facilitating faulting. In a heterogeneous system, the grain sizes of the dehydration products are crucial, which in turn depend on the kinetic mechanism of dehydration. In this study, the reaction of antigorite dehydration to fine-grained forsterite and large talc crystals is controlled by a heterogeneous nucleation and growth mechanism. As the temperature increases from 600 to 650 °C, the influence of forsterite by growth control increases (n decreases to close to 1, Fig. 4b), resulting in the formation of finer-grained forsterite. This change indicates that the increase in the dehydration degree in the core of a serpentinized fault zone will facilitate faulting, triggering earthquakes and extending to the more brittle peridotite. Therefore, the reaction of antigorite dehydration to talc, one of the weakest phyllosilicates (Moore and Lockner 2011), and fine-grained forsterite may be responsible for shallow intermediate-depth seismicity in hot subduction zones (Fig. 6).

Acknowledgments and Funding

We thank Tingting Shen for the helpful discussion and guidance during TEM measurement of the modulation structure of antigorite. We also appreciate the valuable comments and suggestions from the two anonymous reviewers and the Associate Editor, Sarah Brownlee, which helped us improve the manuscript. This work was supported by the Strategic Priority Research Program (B) of the Chinese Academy of Sciences (Grant Nos. XDB42020403 and XDB18000000), the National Natural Science Foundation of China (Grant Nos. 41702224 and 41874107), a research grant from the State Key Laboratory of Earthquake Dynamics (Grant No. LED2017B06), and the Pearl River Talent Plan of Guangdong Province. This is a contribution to No. IS-3122 from GIGCAS.

References cited

Abers, G.A., Nakajima, J., van Keken, P.E., Kita, S., and Hacker, B.R. (2013) Thermal-petrological controls on the location of earthquakes within subducting plates. Earth and Planetary Science Letters, 369-370, 178–187.

Auzende, A.-L., Devouard, B., Guillot, S., Daniel, I., Baronnet, A., and Lardeaux, J.-M. (2002) Serpentinites from Central Cuba: Petrology and HRTEM study. European Journal of Mineralogy, 14, 905–914.

Avrami, M. (1939) Kinetics of phase change. The Journal of Chemical Physics, 7, 1103–1112.

Balucan, R.D., Kennedy, E.M., Mackie, J.F., and Dlugogorski, B.Z. (2011) Optimization of antigorite heat pre-treatment via kinetic modeling of the dihydroxylation reaction for CO_2 mineralization. Greenhouse Gases: Science and Technology, 1, 294–304.

Barcheck, C.G., Wiens, D.A., van Keken, P.E., and Hacker, B.R. (2012) The relationship of intermediate- and deep-focus seismicity to the hydration and dehydration of subducting slabs. Earth and Planetary Science Letters, 349-350, 153–160.

Boettcher, M.S., Hirth, G., and Evans, B. (2007) Olivine friction at the base of oceanic seismogenic zones. Journal of Geophysical Research, 112. http://doi.org/10.1029/2006JB004301.

Bose, K., and Ganguly, J. (1995) Experimental and theoretical studies of the stabilities of talc, antigorite and phase A at high pressures with applications to subduction processes. Earth and Planetary Science Letters, 136, 109–121.

Brantut, N., Stefanou, I., and Sulem, J. (2017) Dehydration-induced instabilities at intermediate-depths in subduction zones. Journal of Geophysical Research,

Downloaded from http://pubs.geoscienceworld.org/msa/ammin/article-pdf/108/1/127/5755349/am-2022-8271.pdf
by Institute of Geochemistry Chinese Academy user
on 12 June 2024

122, 6087–6107.
Bromiley, G.D., and Pawley, A.R. (2003) The stability of antigorite in the system $MgO\text{-}SiO_2\text{-}H_2O$ (MSH) and $MgO\text{-}Al_2O_3\text{-}SiO_2\text{-}H_2O$ (MASH): the effects of Al^{3+} substitution on high-pressure stability. American Mineralogist, 88, 99–108.
Cahn, J.W. (1956) The kinetics of grain boundary nucleated reactions. Acta Metallurgica, 4, 449–459.
Candela, P.A., Crummett, C.D., Earnest, D.J., Frank, M.R., and Wylie, A.G. (2007) Low-pressure decomposition of chrysotile as a function of time and temperature. American Mineralogist, 92, 1704–1713.
Chernak, L.J., and Hirth, G. (2010) Deformation of antigorite serpentinite at high temperature and pressure. Earth and Planetary Science Letters, 296, 23–33.
——— (2011) Syndeformational antigorite dehydration produces stable fault slip. Geology, 39, 847–850.
Chollet, M., Daniel, I., Koga, K.T., Morard, G., and Moortele, B. (2011) Kinetics and mechanism of antigorite dehydration: implications for subduction zone seismicity. Journal of Geophysical Research, 116. doi:10.1029/2010JB007739.
Christian, J.W. (1975) Transformations in Metals and Alloys. Pergamon.
Debret, B., Bolfan-Casanova, N., Padrón-Navarta, J.A., Martin-Hernandez, F., Andreani, M., Garrido, C.J., López Sánchez-Vizcaíno, V., Gómez-Pugnaire, M.T., Muñoz, M., and Trcera, N. (2015) Redox state of iron during high-pressure serpentinite dehydration. Contributions to Mineralogy and Petrology, 169.
Dobson, D.P., Meredith, P.G., and Boon, S.A. (2002) Simulation of subduction zone seismicity by dehydration of serpentine. Science, 298, 1407–1410.
Dunkel, K.G., Austrheim, H., Renard, F., Cordonnier, B., and Jamtveit, B. (2017) Localized slip controlled by dehydration embrittlement of partly serpentinized dunites, Leka Ophiolite complex, Norway. Earth and Planetary Science Letters, 463, 277–285.
Evans, B.W., Johannes, W., Oterdoom, H., and Trommsdorff, V. (1976) Stability of chrysotile and antigorite in the serpentinite multisystem. Schweizerische Mineralogische und Petrographische Mitteilungen, 56, 79–93.
Ferrand, T.P. (2019) Seismicity and mineral destabilizations in the subducting mantle up to 6 GPa, 200 km depth. Lithos, 334-335, 205–230.
Ferrand, T.P., Hilairet, N., Incel, S., Deldicque, D., Labrousse, L., Gasc, J., Renner, J., Wang, Y., Green, H.W.I., and Schubnel, A. (2017) Dehydration-driven stress transfer triggers intermediate-depth earthquakes. Nature Communications, 8, 15247.
French, M.E., Hirth, G., and Okazaki, K. (2019) Fracture-induced pore fluid pressure weakening and dehydration of serpentinite. Tectonophysics, 767, 228168.
Garth, T., and Rietbrock, A. (2014) Order of magnitude increase in subducted H_2O due to hydrated normal faults within the Wadati-Benioff zone. Geology, 42, 207–210.
Gasc, J., Schubnel, A., Brunet, F., Guillon, S., Mueller, H.-J., and Lathe, C. (2011) Simultaneous ascoustic emissions monitoring and synchrotron X-ray diffraction at high pressure and temperature: Calibration and application to serpentinite dehydration. Physics of the Earth and Planetary Interiors, 189, 121–133.
Gasc, J., Hilairet, N., Yu, T., Ferrand, T., Schubnel, A., and Wang, Y. (2017) Faulting of natural serpentinite: Implications for intermediate-depth seismicity. Earth and Planetary Science Letters, 474, 138–147.
Gualtieri, A.F., Giacobbe, C., and Viti, C. (2012) The dihydroxylation of serpentine group minerals. American Mineralogist, 97, 666–680.
Guillot, S., Hattori, K.H., and de Sigoyer, J. (2000) Mantle wedge serpentinization and exhumation of eclogites insights from eastern Ladakh, northwest Himalaya. Geology, 28, 199–202.
Hess, H.H., Smith, R.J., and Dengo, G. (1952) Antigorite form the vicinity of Caracas, Venezuela. American Mineralogist, 37, 68–75.
Hilairet, N., Daniel, I., and Reynard, B. (2006) Equation of state of antigorite, stability field of serpentines, and seismicity in subduction zones. Geophysical Research Letters, 33, L02302.
Hilairet, N., Reynard, B., Wang, Y., Daniel, I., Merkel, S., Nishiyama, N., and Petitgirard, S. (2007) High-pressure creep of serpentine, interseismic deformation, and initiation of subduction. Science, 318, 1910–1913.
Huang, R.F., Lin, C.-T., Sun, W.D., Ding, X., Zhan, W.H., and Zhu, J.H. (2017) The production of iron oxide during peridotite serpentinization: Influence of pyroxene. Geoscience Frontiers, 8, 1311–1321.
Hushur, A., Manghnani, M.H., Smyth, J.R., Nestola, F., and Frost, D.J. (2009) Crystal chemistry of hydrous forsterite and its vibrational properties up to 41 GPa. American Mineralogist, 94, 751–760.
Hyndman, R.D., and Peacock, S.M. (2003) Serpentinization of the forearc mantle. Earth and Planetary Science Letters, 212, 417–432.
Inoue, T., Yoshimi, I., Yamada, A., and Kikegawa, T. (2009) Time-resolved X-ray diffraction analysis of the experimental dehydration of serpentine at high pressure. Journal of Mineralogical and Petrological Sciences, 104, 105–109.
Ji, S., Li, A.W., Wang, Q., Long, C.X., Wang, H.C., Marcotte, D., and Salisbury, M.H. (2013) Seismic velocities, anisotropy, and shear-wave splitting of antigorite serpentinites and tectonic implications for subduction zones. Journal of Geophysical Research, 118, 1015–1037.
Jung, H., Green, H.W II, and Dobrzhinetskaya, L.F. (2004) Intermediate-depth earthquake faulting by dehydration embrittlement with negative volume change. Nature, 428, 545–549.
King, D.S.H., and Marone, C. (2012) Friction properties of olivine at high temperature with applications to the strength and dynamics of the oceanic lithosphere. Journal of Geophysical Research, 117. http://doi.org/10.1029/2012JB009511.
Liu, T., Wang, D.J., Shen, K.W., Liu, C.J., and Yi, L. (2019) Kinetics of antigorite dehydration: Rapid dehydration as a trigger for lower-plane seismicity in subduction zones. American Mineralogist, 104, 282–290.
Llana-Fúnez, S., Brodie, K.H., Rutter, E.H., and Arkwright, J.C. (2007) Experimental dehydration kinetics of serpentinite using pore volumometry. Journal of Metamorphic Geology, 25, 423–438.
Merkulova, M., Munoz, M., Vidal, O., and Brunet, F. (2016) Role of iron content on serpentinite dehydration depth in subduction zones: Experiments and thermodynamic modeling. Lithos, 264, 441–452.
Miller, S.A., van der Zee, W., Olgaard, D.L., and Connolly, J.A.D. (2003) A fluid-pressure feedback model of dehydration reactions: Experiments, modelling, and application to subduction zones. Tectonophysics, 370, 241–251.
Moore, D.E., and Lockner, D.A. (2011) Frictional strengths of talc-serpentine and talc-quartz mixture. Journal of Geophysical Research, 116, B01403.
Okazaki, K., and Hirth, G. (2016) Dehydration of lawsonite could directly trigger earthquakes in subducting oceanic crust. Nature, 530, 81–84.
Okazaki, K., and Katayama, I. (2015) Slow stick slip of antigorite serpentinite under hydrothermal conditions as a possible mechanism for slow earthquakes. Geophysical Research Letters, 42, 1099–1104.
Omori, S., Komabayashi, T., and Maruyama, S. (2004) Dehydration and earthquakes in the subducting slab: empirical link in intermediate and deep seismic zones. Physics of the Earth and Planetary Interiors, 146, 297–311.
Padrón-Navarta, J.A., López Sánchez-Vizcaíno, V., Garrido, C.J., Gómez-Pugnaire, M.T., Jabaloy, A., Capitani, G., and Mellini, M. (2008) Highly ordered antigorite from Cerro del Almirez HP-HT serpentinites. Contributions to Mineralogy and Petrology, 156, 679–688.
Padrón-Navarta, J.A., López Sánchez-Vizcaíno, V., Hermann, J., Connolly, J.A.D., Garrido, C.J., Gómez-Pugnaire, M.T., and Marchesi, C. (2013) Tschermak's substitution in antigorite and consequences for phase relations and water liberation in high-grade serpentinites. Lithos, 178, 186–196.
Peacock, S.M. (2001) Are the lower planes of double seismic zones caused by serpentine dehydration in abducting oceanic mantle? Geology, 29, 299–302.
Perrillat, J.-P., Daniel, I., Koga, K.T., Reynard, B., Cardon, H., and Crichton, W.A. (2005) Kinetics of antigorite dehydration: A real-time X-ray diffraction study. Earth and Planetary Science Letters, 236, 899–913.
Proctor, B., and Hirth, G. (2015) Role of pore fluid pressure on transient strength changes and fabric development during serpentine dehydration at mantle conditions: Implications for subduction-zone seismicity. Earth and Planetary Science Letters, 421, 1–12.
Raleigh, C.B., and Paterson, M.S. (1965) Experimental deformation of serpentinite and its tectonic implications. Journal of Geophysical Research, 70, 3965–3985.
Rayner, J.H., and Brown, G. (1973) The crystal structure of talc. Clays and Clay Minerals, 21, 103–114.
Reynard, B. (2013) Serpentine in active subduction zones. Lithos, 178, 171–185.
Reynard, B., Hilairet, N., Balan, E., and Lazzeri, M. (2007) Elasticity of serpentines and extensive serpentinization in subduction zones. Geophysical Research Letters, 34, L13307.
Rinaudo, C., Gastaldi, D., and Belluso, E. (2003) Characterization of chrysotile, antigorite and lizardite by FT-RAMAN spectroscopy. Canadian Mineralogist, 41, 883–890.
Rubie, D.C., and Thompson, A.B. (1985) Kinetics of metamorphic reactions at elevated temperatures and pressures: An appraisal of available experimental data. In A.B. Thompson and D.C. Rubie, Eds., Metamorphic Reactions: Kinetics, Textures, and Deformation, p. 27–29. Springer.
Rutter, E.H., and Brodie, K.H. (1988) Experimental "sytectonic" dehydration of serpentinite under conditions of controlled pore water pressure. Journal of Geophysical Research: Solid Earth, 93, 4907–4932.
Rutter, E.H., Llana-Fúnez, S., and Brodie, K.H. (2009) Dehydration and deformation of intact cylinders of serpentinite. Journal of Structural Geology, 31, 29–43.
Sawai, M., Katayama, I., Hamada, A., Maeda, M., and Nakashima, S. (2013) Dehydration kinetics of antigorite using in situ high-temperature infrared microspectroscopy. Physics and Chemistry of Minerals, 40, 319–330.
Scambelluri, M., Müntener, O., Hermann, J., Piccardo, G.B., and Trommsdorff, V. (1995) Subduction of water into the mantle: History of an Alpine peridotite. Geology, 23, 459–462.
Schmidt, M.W., and Poli, S. (1998) Experimentally based water budgets for dehydrating slabs and consequences for arc magma generation. Earth and Planetary Science Letters, 163, 361–379.
Schubnel, A., Brunet, F., Hilairet, N., Gasc, J., Wang, Y., and Green, H.W. (2013) Deep-focus earthquake analogs recorded at high pressure and temperature in the laboratory. Science, 341, 1377–1380.
Shao, T., Ji, S., Kondo, Y., Michibayashi, K., Wang, Q., Xu, Z., Sun, S., Marcotte, D., and Salisbury, M.H. (2014) Antigorite-induced seismic anisotropy and implications for deformation in subduction zones and the Tibetan Plateau. Journal of Geophysical Research: Solid Earth, 119, 2068–2099.
Shao, T., Zhou, Y., Song, M., Ma, X., Zhang, L., Yao, W., Dang, J., and Li, J.F.

Downloaded from http://pubs.geoscienceworld.org/msa/ammin/article-pdf/108/1/127/5755349/am-2022-8271.pdf
by Institute of Geochemistry Chinese Academy user
on 12 June 2024

(2021) Deformation of antigorite and its geological implications. Journal of Geophysical Research, 126. https://doi.org/10.1029/2021JB021650.

Shao, T., Song, M., Li, J.F., Wu, J., Zhou, Y.S., Ma, X., and Ding, X. (2022) Mechanical behaviors of intact antigorite as functions of temperature: Faulting, slow stick-slip and stable sliding. Journal of Structural Geology, 158. http://doi.org/10.1016/j.jsg.2022.104579.

Shen, T., Zhang, C., Chen, J., Hermann, J., Zhang, L., Padrón-Navarta, J.A., Chen, L., Xu, J., and Yang, J. (2020) Changes in the cell parameters of antigorite close to its dehydration reaction at subduction zone conditions. American Mineralogist, 105, 569–582.

Takahashi, M., Uehara, S.-I., Mizoguchi, K., Shimizu, I., Okazaki, K., and Masuda, K. (2011) On the transient response of serpentine (antigorite) gouge to stepwise changes in slip velocity under high-temperature conditions. Journal of Geophysical Research, 116, B10405.

Taylor, L.S., and York, P. (1998) Effect of particle size and temperature on the dehydration kinetics of trehalose dehydrate. International Journal of Pharmaceutics, 167, 215–221.

Ulmer, P., and Trommsdorff, V. (1995) Serpentine stability to mantle depths and subduction-related magmatism. Science, 268, 858–861.

——— (1999) Phase relations of hydrous mantle subducting to 300 km. Conference Paper, Geochemical Society, pp. 259–282.

Wang, D., Wang, Y., Yi, L., and Huang, B. (2015) Dehydration kinetics of natural talc. Canadian Mineralogist, 53, 643–651.

Weber, J.N., and Greer, R.T. (1965) Dehydration of serpentine: Heat of reaction and reaction kinetics at $P_{H_2O} = 1$ atm. American Mineralogist, 50, 450–464.

Wunder, B., and Schreyer, W. (1997) Antigorite: High-pressure stability in the system MgO-SiO_2-H_2O (MSH). Lithos, 41, 213–227.

Wunder, B., Baronnet, A., and Schreyer, W. (1997) Ab-initio synthesis and TEM confirmation of antigorite in the system MgO-SiO_2-H_2O. American Mineralogist, 82, 760–764.

Wunder, B., Wirth, R., and Gottschalk, M. (2001) Antigorite: Pressure and temperature dependence of polysomatism and water content. European Journal of Mineralogy, 13, 485–495.

Xia, G. (2013) Experimental studies on dehydration embrittlement of serpentinized peridotite and effect of pressure on creep of olivine. Ph.D. dissertation, University of California.

Yamasaki, T., and Seno, T. (2003) Double seismic zone and dehydration embrittlement of the subducting slab. Journal of Geophysical Research, 108. doi:10.1029/2002JB001918.

Zhang, Z., and Duan, Z. (2005) Prediction of the PVT properties of water over wide range of temperatures and pressures from molecular dynamics simulation. Physics of the Earth and Planetary Interiors, 149, 335–354.

Manuscript received August 24, 2021
Manuscript accepted January 19, 2022
Accepted manuscript online January 26, 2022
Manuscript handled by Sarah Brownlee

Endnote:

[1]Deposit item AM-23-18271, Online Materials. Deposit items are free to all readers and found on the MSA website, via the specific issue's Table of Contents (go to http://www.minsocam.org/MSA/AmMin/TOC/2023/Jan2023_data/Jan2023_data.html).

Downloaded from http://pubs.geoscienceworld.org/msa/ammin/article-pdf/108/1/127/5755349/am-2022-8271.pdf
by Institute of Geochemistry Chinese Academy user
on 12 June 2024